Resonance-Raman and lattice-dynamics studies of single-crystal PdO

J. R. McBride, K. C. Hass, and W. H. Weber
Research Staff, Ford Motor Company, Dearborn, Michigan 48121
(Received 27 March 1991)

Polarized Raman measurements are performed on oriented single crystals of PdO, grown by a vapor-transport technique. The allowed Raman modes, B_{1g} and E_g, are assigned to lines at 651 and 445 cm^{-1}, respectively. Intensity–versus–excitation-wavelength profiles for these lines show a strong resonance behavior, the presence of which leads to the appearance of numerous additional features in the spectrum. By fitting these profiles to an exciton model of resonant Raman scattering we obtain $\hbar\omega_{ex}=2.423\pm0.011$ and $\hbar\Gamma=0.071\pm0.018$ eV for the exciton energy and half-width. Both the position and width match well a prominent peak in Im(ϵ) appearing in the PdO optical properties reported by Nilsson and Shivaraman [J. Phys. C **12**, 1423 (1979)]. Phonon-dispersion curves and the density of states are calculated with a simple valence-force model incorporating the important bond-stretching and -bending motions. With these calculations and with results from experiments on isotopically substituted $Pd^{18}O$, we are able to assign most of the additional features in the Raman spectrum to second-order scattering from overtones and combinations or to forbidden LO-phonon scattering. The overtone of the B_{1g} mode appears as a sharp line in the spectrum, very similar to the case for the single Raman-active mode in diamond.

I. INTRODUCTION

Palladium oxide (PdO) is known to be a *p*-type semiconductor. Despite the technological interest in this compound both as a dehydrogenation catalyst and as a photocathode in water electrolysis, there is little detailed knowledge of its electronic properties. Even the band gap of PdO is not firmly established. Okamoto and Aso[1] prepared polycrystalline films by oxidizing evaporated Pd layers and concluded on the basis of conductivity versus temperature data that the band gap was near 1.5 eV. Rogers *et al.*[2] grew single crystals of PdO and found much higher resistivities than Okamoto and Aso. Their conductivity results were dominated by defects, however, and they were unable to determine a band gap. Rey *et al.*[3] made semitransparent polycrystalline samples by oxidizing sputtered Pd films and reported values of 2.13 eV for the gap, based on the extrapolated optical density, and 2.67 eV, based on the photoconductivity edge. Nilsson and Shivaraman[4] studied similarly prepared PdO films and determined the optical constants by Kramers-Kronig analysis of transmittance data over the range 0.5–5.4 eV. They found a small band gap of 0.8 eV with only a weakly increasing absorbance just above this value. The most striking feature in the optical properties is a strong peak in Im(ϵ) occurring at $\sim$2.5 eV. This feature is responsible for the orange color of the semitransparent films and the greenish blue color of the single crystals or the thin oxides on bulk Pd.

In the PdO structure, Pd^{2+} ions are planar coordinated by four O^{2-} ions. This configuration, with oxygen surrounding a *d*-band metal, is also found in CuO and most of the high-T_c superconductors. The belief that interactions between Cu and O atoms in CuO_2 planes is fundamental to the occurrence of superconductivity has generated a large amount of interest in the study of phonons in these materials.[5–7] Optical phonons have been studied in PdO by Kliche[8] using far-infrared reflectivity and by Weber *et al.*[9] using Raman scattering. The former yielded frequencies for the three ir-active modes ($A_{2u}+2E_u$), and the latter tentative frequencies for the two Raman-active modes ($B_{1g}+E_g$). The Raman results were complicated by a strong resonance effect that led to the appearance of many extra lines in the spectrum. Since the experiments were performed on polycrystalline samples, no symmetry-species assignments for the vibrational modes could be made by polarization measurements. However, Kliche[10] has recently used a simple force-constant analysis of the zone-center phonons to assign the infrared and B_{1g} Raman-active modes. The primary purposes of this paper are to obtain polarized Raman spectra from oriented single crystals, to study the resonance enhancement of the different phonons, to provide an analysis of the complex Raman spectrum that is observed near the resonance peak, and to correlate the resonance results with the electronic structure.

The paper is organized as follows: Section II discusses the experimental details regarding sample preparation and Raman measurements. Section III describes the structure and bonding in PdO and enumerates the zone-center optical phonons. Section IV presents the polarized Raman spectra, resonance data for both modes, and spectra from ^{18}O-substituted films. Section V gives results of lattice-dynamics calculations, which lead to the assignments for most of the second-order scattering, described in Sec. VI. Section VII provides a discussion and summary.

II. EXPERIMENTAL DETAILS

Single crystals of PdO were grown by a vapor-transport technique similar to that previously described.[2,11] Starting powders obtained from Johnson Matthey were pretreated by heating the PdO in flowing oxygen at 800 °C and drying the $PdCl_2$ in air at 300 °C. Approximately equal portions by weight of the powders were loaded into quartz ampules (2.2-cm o.d. by 20-cm length), evacuated, and sealed. The ampules were placed in a two-zone, computer-controlled furnace and brought to temperature with the charge zone maintained at 825 °C and the growth zone at 900 °C. After 75 h, the furnace was slowly cooled at a rate of 7 °C/h. Upon examination of the cooled ampules, lustrous metallic-green crystals of PdO were found adhering to the tube walls in the growth zone. In addition, red crystals, presumably $PdCl_2$, were found in the charge zone near the unreacted flux. A variety of PdO crystal sizes were present, dependent upon the position within the growth zone, with the largest samples having facets several mm on edge. X-ray analyses were performed to confirm the structure and orient several of the larger crystals. The preferred growth habit tended to yield (001) facets; however, we occasionally found exceptions such as the crystal with a large (110) facet shown in Fig. 1. We also noted interesting cases where large PdO crystals grew by forming shells over droplets of flux attached to the tube walls. The flux trapped in these "hollow" PdO crystals was removed by etching. The PdO crystals were extremely inert, being insoluble in all the acids tested. Several of the PdO samples were potted in epoxy and polished with 1-μm diamond paste to produce high-quality optical surfaces. Unfortunately, the Raman spectra obtained after polishing were worse than the original spectra taken from the same crystals. Reduced signal strength, broadened line widths, and the absence of weak features in the spectra suggest that mechanical damage was caused by polishing. Consequently, all the Raman data reported here were obtained on as-grown facets.

Additional PdO samples were prepared by oxidizing foils and sputtered films. The sputtered samples, 1-μm-thick Pd films deposited on quartz, were completely oxidized by heating them in air for 18 h at 650 °C. The Pd foils were heated in vacuum by passing a current through them. After an initial period at high temperature to clean the surfaces, the foils were cooled to about 600 °C and oxygen was introduced at 150 Torr for 1 h. This method produced oxide layers roughly a few hundred Å thick.[9] By using $^{18}O_2$ gas (97% atomic purity) we were able to grow identical films of isotopically enriched $Pd^{18}O$.

The Raman spectra were obtained using the lines from Ar^+ ion and HeNe lasers, a SPEX triplemate spectrometer, and a 1024-element intensified solid-state array detector operated at −30 °C. The incident beam was s polarized and focused on the sample at 65° from the normal. The scattered light was collected normal to the surface with a camera lens at $\sim f/2$. An analyzer was placed between the camera lens and the spectrometer for polarization measurements.

III. STRUCTURE AND MODES

PdO and the closely related compounds PtO and PtS crystallize in the tetragonal cooperite structure[12] (D^9_{4h}, $Z=2$) as shown in Fig. 2. A factor-group analysis[8,9] of the zone-center optical phonons for this structure yields three ir-active modes, species $A_{2u}+2E_u$; two Raman-active modes, species $B_{1g}+E_g$; and one silent mode, species B_{2u}. The A_{2u} mode is polarized along the c axis and the two E_u modes perpendicular to the c axis. The scattering tensor for the B_{1g} mode has nonzero components $\alpha_{xx}=-\alpha_{yy}$, that for the E_g mode has nonzero components $\alpha_{xz}=\alpha_{yz}$. The eigenvectors for the Raman-active modes are shown in Fig. 2. Both modes involve only O motion, which is parallel to the c axis for B_{1g} and perpendicular to it for E_g.

In the PdO structure, the Pd atoms are planar coordinated with four O's, while the O's are tetrahedrally coordinated with four Pd's as shown in Fig. 3. A qualitative picture of the electronic structure has been given by

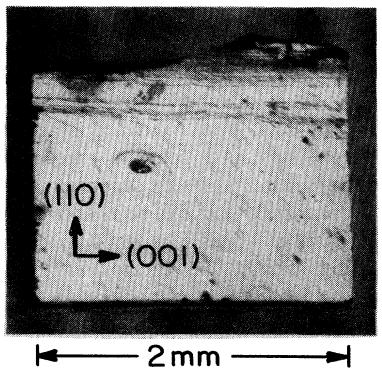

FIG. 1. Photograph of PdO crystal with large (110) face.

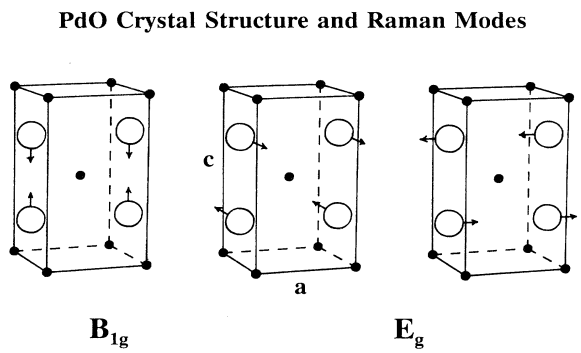

FIG. 2. Crystal structure and Raman-active modes of PdO. Palladium atoms (small circles) occupy D_{2h} sites. Oxygen atoms (large circles) occupy D_{2d} sites and are responsible for the allowed Raman modes. Lattice constants are $a=3.043$ Å and $c=5.3367$ Å.

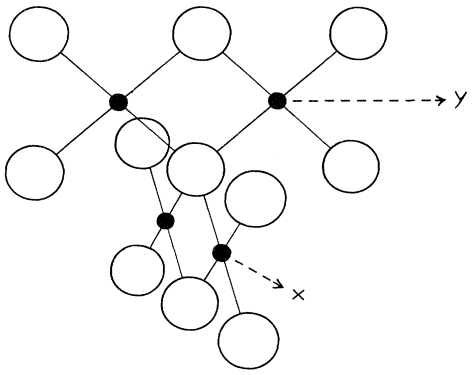

FIG. 3. Diagram showing the bond coordination in PdO. The Pd atoms (small circles) are planar coordinated by four O atoms (large circles); the O atoms are tetrahedrally coordinated by four Pd atoms.

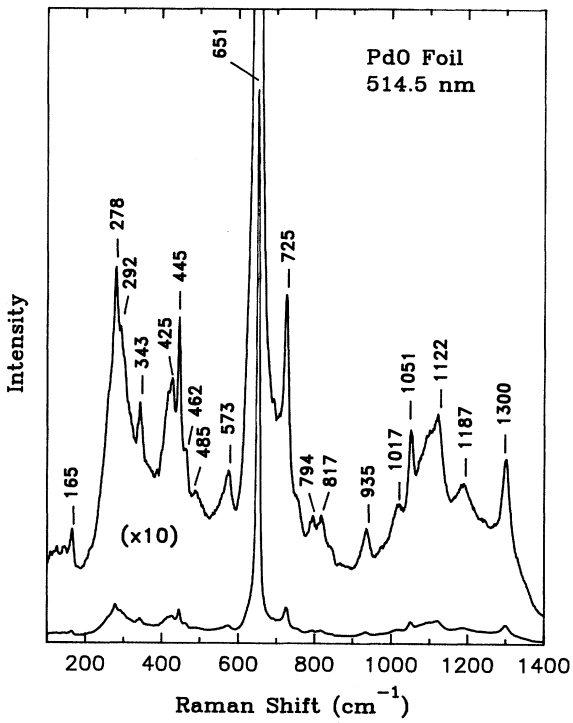

FIG. 4. Unpolarized Raman spectra of a typical PdO sample obtained using the 514.5-nm laser line at 100 mW. The peak signal is ~150 counts/s. The upper curve is a magnification of the lower one and has frequencies of the most prominent features labeled for reference.

several authors.[2,11,13] The Pd atom has a formal valence of +2, yielding a $4d^8$ configuration, while the O has −2, yielding $2p^6$. The valence band is formed by the filled O $2p$ states, which are hybridized with the Pd $4d$ states of local symmetries a_{1g}, b_{2g}, and e_g. The lowest states in the conduction band are associated with the empty Pd $4d$ states of b_{1g} symmetry. These are antibonding states whose wave functions are oriented toward the neighboring O's. Theoretical support for this picture has come from the cluster calculations of Gagarin *et al.*,[14] and experimental support from the photoemission studies by Holl *et al.*[15]

IV. RESULTS

A. Polarized spectra on single crystals

The Raman spectrum from a typical unoriented PdO sample is shown in Fig. 4. This spectrum, taken from an oxidized foil, is virtually identical to those taken from oxidized sputtered films and randomly oriented single crystals. Since different preparation techniques were used to produce these samples, we conclude that the large number of features appearing in the spectrum are intrinsic to PdO and are not due to contaminants. Frequencies for most of the prominent features have been labeled in the figure for reference. On the basis of more than 200 spectra that have been recorded, we have found that all of the recognizable features are reproducible, including the small details that have not been labeled in the figure.

The two allowed Raman modes were identified with spectra taken from oriented single crystals. With an s-polarized incident beam, the Raman tensor symmetries allow only the B_{1g} mode when scattering from an (001) face and only the E_g mode when scattering from a (110) face. These assertions are verified by the spectra shown in Figs. 5 and 6. The spectra here were obtained using the 457.9-nm laser line in order to reduce the strength of additional features caused by resonance effects. In each figure the depolarized spectrum has been corrected for the difference in throughput of the spectrometer for the different polarizations. Relative intensities can thus be directly compared. In Fig. 5 the single strong line found at 651 cm^{-1} in the $x'y'$ polarization does not appear in the $x'x'$ polarization and is thus assigned to the B_{1g} mode. Primed coordinates correspond to the [110] directions, i.e., they are obtained from the unprimed ones by a 45° rotation about the c axis. Similarly, the strong line at 445 cm^{-1} in the $x'z$ polarization of Fig. 6 vanishes in the zz polarization and is assigned to the E_g mode.

B. Resonance profiles

The resonant behavior of the allowed Raman modes was investigated at ten excitation frequencies for single crystal, oxidized foil, and oxidized sputtered film samples. The intensities and peak positions of the Raman lines were determined at each wavelength by fitting the peaks to a Lorentzian line shape that included a linearly varying background. This fitting procedure was particularly important for the E_g mode, which usually had a large and sloping background. To correct these data for changes in the spectral response of the system and the ω^4 dependence of the Raman effect, the measured intensities were normalized to those obtained under identical conditions from BaF_2, a transparent material whose Raman polarizability is nearly constant in the visible. In addi-

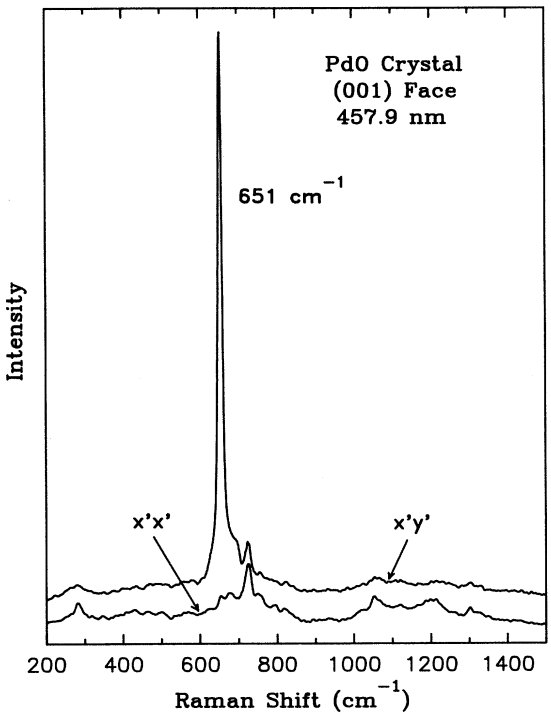

FIG. 5. Polarized scattering from the (001) face of a PdO single crystal. Primed coordinates correspond to the [110] directions. The peak at 651 cm^{-1} is assigned to the B_{1g} mode. Spectra were obtained using the 457.9-nm laser line at 100 mW. The peak signal is ~10 counts/s, and the baseline for the $x'y'$ spectrum has been shifted up by 0.5 counts/s for clarity.

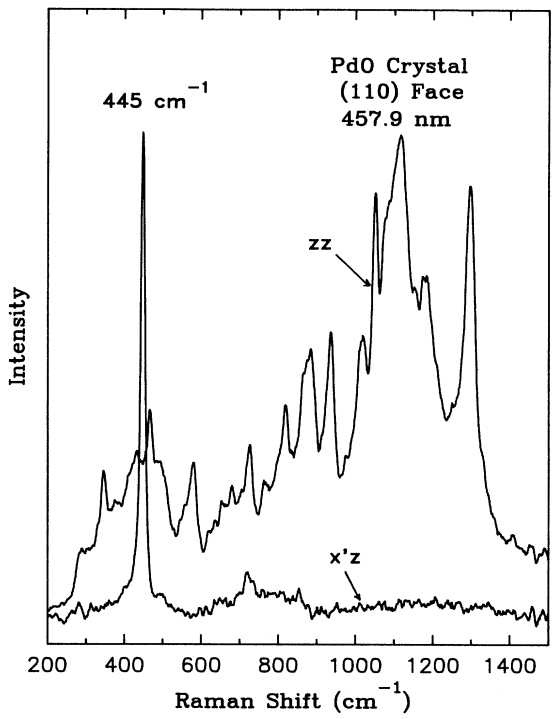

FIG. 6. Polarized scattering from the (110) face of a PdO single crystal. The peak at 445 cm^{-1} is assigned to the E_g mode. Same conditions as for Fig. 5 except the peak signal is ~1 count/s.

tion, it was necessary to correct the data for the variation in the optical properties of PdO, which is considerable over the frequency range of the measurements. This correction was made by dividing the PdO signal strength by

$$F=|t_{12}|^2|t'_{21}|^2[2\,\mathrm{Im}(k_2)+2\,\mathrm{Im}(k'_2)]^{-1}(1-\cos\theta'_2)\ , \quad (1)$$

where t_{12} and t'_{21} are the s-polarized Fresnel amplitude transmission coefficients for the incident and Raman-scattered beams at the PdO (medium 2) surface;[16] k_2 and k'_2 are the normal components of the propagation vectors in medium 2 for the incoming and Raman-scattered beams, respectively, and θ'_2 is the acceptance angle for the collection lens measured in medium 2. The first factor accounts for the reflection loss of the incident beam. The second factor accounts for the reflection loss of the exit beam, which, for simplicity, is evaluated for normal incidence. The third factor is the effective sampling depth obtained by integrating the exponentially attenuated fields over a semi-infinite sample. The last factor reduces to $1/n^2$ for small angles and accounts for the change in the collection angle as the PdO refractive index n changes with wavelength. The factor F was calculated using the optical data from Nilsson and Shivaraman.[4] Their data were obtained from polycrystalline films and do not contain information on the anisotropy expected for the tetragonal structure. However, the nature of the bonding in PdO suggests that the anisotropies will be small, and our subsequent results showing little difference between oriented single crystals and polycrystalline films support this assertion.

Figures 7 and 8 show the resonance data obtained from oxidized foils for the B_{1g} and E_g modes. Similar results were found for other PdO samples. The vertical scale in each figure has been chosen so that the peak corresponds to the maximum observed PdO-to-BaF_2 Raman signal ratio in percent. The remaining points are scaled by the relative changes in F, which changes by nearly a factor of 10 over the range of the data. The dominant factor in F is the sampling depth, which varies from ~100 Å near the resonance peak to ~600 Å at 1.96 eV.

The solid lines in the figures result from a least-squares fit to a model describing a one-phonon Raman-scattering process near an exciton,[17] given by

$$I(\omega)=\left|\frac{1}{(\omega-\omega_{\mathrm{ex}}+i\Gamma)(\omega-\omega_{\mathrm{ex}}-\omega_{\mathrm{ph}}+i\Gamma)}+A(\omega)\right|^2\ , \quad (2)$$

where ω_{ex} is the exciton frequency, ω_{ph} is the phonon frequency, Γ is a phenomenological broadening parameter, and $A(\omega)$ is a background term due to other optical tran-

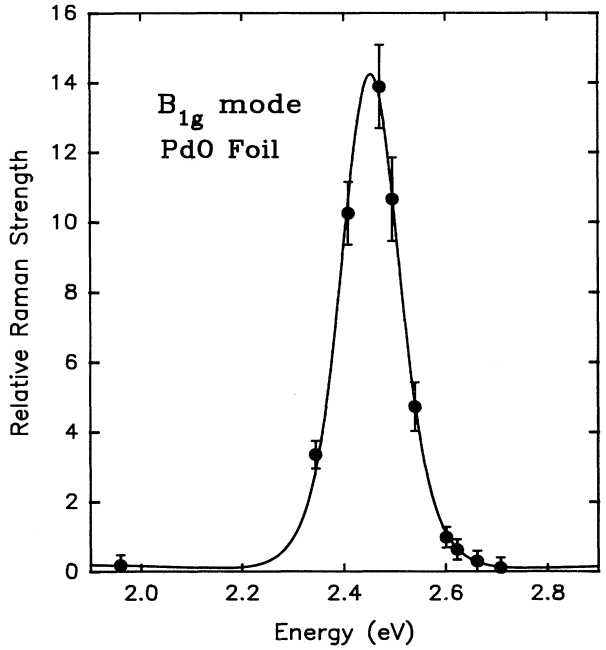

FIG. 7. Resonant-Raman profile of the B_{1g} mode taken from an oxidized foil PdO sample. The vertical scale has been chosen such that the peak point corresponds to the maximum observed PdO-to-BaF_2 ratio in percent. The solid line is a fit to Eq. (2) and yields $\hbar\omega_{ex}=2.413$ eV, $\hbar\Gamma=0.094$ eV.

sitions. The fits were done using a constant real value for A. Note that the position and width of the exciton peak is nearly the same for both modes. Based on results from five complete resonance profiles, the E_g mode exciton

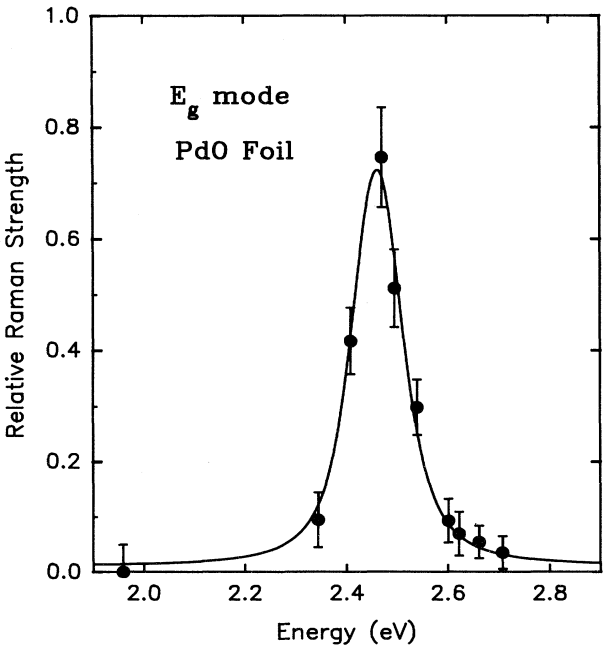

FIG. 8. Resonant-Raman profile of the E_g mode taken from an oxidized foil PdO sample. Same conditions as for Fig. 7. The fit to Eq. (2) yields $\hbar\omega_{ex}=2.434$ eV, $\hbar\Gamma=0.070$ eV.

peak was ~1% higher than that for the B_{1g} mode, which we do not consider significant. The simple average of these measurements, three for B_{1g} and two for E_g, gives $\hbar\omega_{ex}=2.423\pm0.011$ eV and $\hbar\Gamma=0.071\pm0.018$ eV.

Although it is not readily apparent from the resonance profiles, the B_{1g}-to-E_g ratio changes across the energy spectrum. At high energies this ratio is ~6, and at the lowest energies is ≥ 200. (The E_g mode was barely observable at 632.8 nm.) The E_g mode was found to need a larger background term A in all of the resonance fits. This observation, along with the varying B_{1g}-to-E_g ratio, suggests that the background interferes destructively with the E_g mode below the resonance and constructively above it. This background effect may account for the small shift in the exciton energy (~0.02 eV) observed for the E_g mode. A Fano-type line shape might be more appropriate, however, considering the large error bars and the limited data set, such a refinement to the fits is simply not warranted.

Although all the spectral features are observed with each laser line, the general shapes of the spectra are affected by the outgoing photon resonance contained in the ω-ω_{ex}-ω_{ph} term of Eq. (2). For example, when the laser frequency ω is below ω_{ex}, as in Fig. 4, then the features at large Raman shifts are depressed relative to those closer to the laser frequency. Conversely, when ω is above ω_{ex}, as in Fig. 6, then the features at large Raman shifts are relatively more enhanced.

C. $Pd^{18}O$ spectra

In order to confirm the assignments of the Raman modes and to provide clues to the origin of some of the additional features, we measured isotope shifts for foil samples prepared using $^{18}O_2$. A comparison of $Pd^{16}O$ and $Pd^{18}O$ spectra taken at room temperature under identical conditions using the 514.5-nm laser line is shown in Fig. 9. Since both Raman modes involve only oxygen motion, their frequencies should vary as $m_O^{-1/2}$. In the $Pd^{18}O$ spectra, the B_{1g} mode is observed at 613 cm^{-1} and the E_g mode at 420 cm^{-1}, in excellent agreement with the expected behavior. The E_g mode appears more prominent in the $Pd^{18}O$ spectrum, but it is sitting on top of a broader peak at 425 cm^{-1} that does not shift. There is also a definite broadening of some of the $Pd^{18}O$ lines apparent in Fig. 9, which may be the result of some ^{16}O-^{18}O substitutional disorder. This broadening makes the B_{1g} mode appear smaller in the $Pd^{18}O$ spectrum. Two additional peaks appear in the $Pd^{18}O$ spectrum: one at 638 cm^{-1}, to be discussed later, that appears as a shoulder on the high-frequency side of the B_{1g} mode, the other at 462 cm^{-1}, that was nearly obscured by the $Pd^{16}O$ E_g mode. All of the features at frequencies above the B_{1g} mode shift down in the $Pd^{18}O$ spectra by ~5%, whereas features below the B_{1g} mode, excepting E_g, do not appear to shift. As we show in the following section, this behavior results from the fact that the high- and low-frequency phonons involve primarily O and Pd motions, respectively.

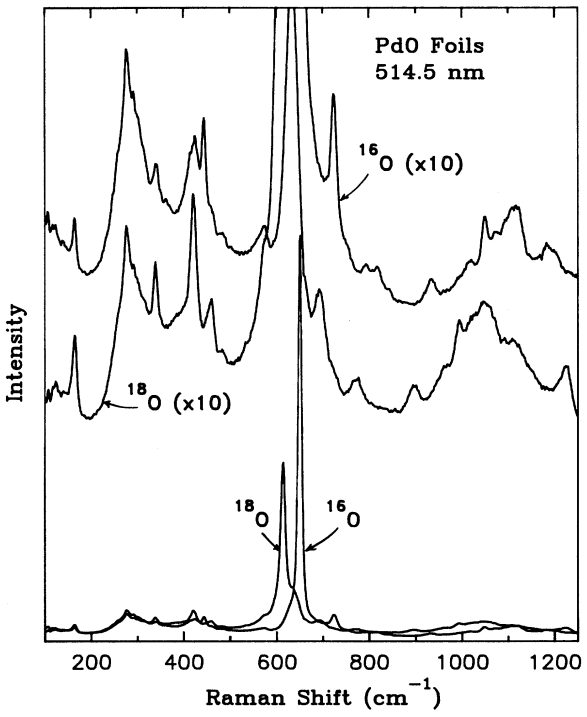

FIG. 9. Raman spectra from Pd^{16}O and Pd^{18}O oxidized foil samples recorded under identical conditions at room temperature. Spectra were obtained using the 514.5-nm laser line at 100 mW. The peak signal is ~280 counts/s.

For completeness, we also measured spectra at 10 K. These were very similar to the room-temperature spectra, with the exception that the Raman lines were narrower. This made it possible to resolve the Pd^{18}O E_g mode from the feature beneath it. The Pd^{16}O and Pd^{18}O B_{1g} modes appear at 657 and 619 cm^{-1}, respectively; the E_g modes at 447 and 422 cm^{-1}, respectively. The small positive frequency shifts of these lines compared with their room-temperature values are consistent with what is expected from thermal expansion effects.

V. LATTICE-DYNAMICS CALCULATIONS

We anticipate that much of the additional structure in the PdO Raman spectrum can be attributed to second-order processes, i.e., scattering in which one phonon at $+\mathbf{q}$ is simultaneously excited with a second phonon at $-\mathbf{q}$. Such a scattering process samples the phonon energies throughout the Brillouin zone, and the resulting spectrum will cover a wide frequency range with numerous peaks corresponding to critical points where the appropriate density of states is high. Our aim in this section is to provide a full lattice-dynamical calculation based on an empirical valence-force model that yields realistic phonon dispersion curves. With these curves we will calculate the second-order overtone spectrum, in which both phonons come from the same branch, and make predictions for certain combination features, in which the phonons come from different branches. These results will then be directly compared with our experiments. Following Kliche,[10] we assume that the dominant interactions in this material are covalent in nature and we neglect the longer-ranged Coulomb forces known to be responsible for the 10–30 cm^{-1} LO-TO splittings observed for the ir-active modes.[8]

Table I lists the experimental zone-center phonon frequencies that we have used as constraints on our parameterizations. The table also gives results for four different theoretical models, including that of Kliche.[10] The Kliche model is based on three bond-stretching force constants: f^1_{PdO}, between Pd and O nearest neighbors; f^2_{PdO}, between next-nearest-neighbor Pd and O pairs; and f_{OO}, between nearest-neighbor O pairs (along the c axis).

TABLE I. Top: Comparison of experimental zone-center phonon frequencies with theoretical values for different models. Bottom: Corresponding values of force constants defined in text.

	Expt. cm^{-1}	Kliche[a] cm^{-1}	Model 1[b] cm^{-1}	Model 2[b] cm^{-1}	Model 3[b] cm^{-1}
E^1_u	165[b]	160	177	179	180
B_{2u}		242	242	246	251
E_g	445[b]	554	445	445	445
E^2_u	612[a]	611	600	597	598
B_{1g}	651[b]	652	651	651	651
A_{2u}	668[a]	668	668	668	668
		eV/Å^2	eV/Å^2	eV/Å^2	eV/Å^2
f^1_{PdO}		12.50	10.30	8.78	7.25
f^2_{PdO}		1.19			
f_{OO}		0.56	−0.71	−1.03	−1.36
k_{O}				0.30	0.60
k_{Pd}			1.09	1.37	1.66
μ			2.07	1.88	1.70

[a]Reference 10.
[b]This work.

With only these parameters, Kliche obtained an excellent fit to all four of the zone-center frequencies known at that time. The present Raman results indicate, however, that the E_g mode in this model is too high by over 100 cm^{-1}. The three stretching forces in this model are also insufficient to prevent a zero-frequency mode from occurring at the R point of the Brillouin zone. The remaining models in Table I thus include two additional bond-bending force constants, k_O and k_{Pd}, for bond angles about O and Pd sites, respectively, and a buckling force constant μ associated with deviations from a planar Pd coordination.[18] This particular choice of valence forces was motivated by the strong directional bonding in Fig. 2. The full dynamical matrix including all of the force constants defined in this paragraph is described in the Appendix.

With the inclusion of the bond-bending and buckling force constants, the problem is overdetermined, there being six parameters to fit five observed frequencies. This redundancy in the full parameter set is eliminated in models 1–3 by setting $f^2_{PdO}=0$. In principle, the five remaining parameters should be sufficient to fit the known zone-center modes exactly. This is indeed possible, but only by choosing $k_O \ll 0$, which leads to an unstable lattice. Non-negative values of k_O are required to ensure that the frequencies associated with shear displacements at the X and Z points of the Brillouin zone are real. Since there is no fully satisfactory way of choosing k_O, we consider a range of values in models 1–3, with the remaining parameters chosen to reproduce the E_g, B_{1g}, and A_{2u} frequencies, and the average of E^1_u and E^2_u. The difference between the observed and calculated frequencies for the E_u modes increases slightly with k_O but is less than 15 cm^{-1} in each of the models. The parametrized bond-bending and buckling force constants turn out to be much smaller than f^1_{PdO}, as in most other systems.[19] The only potentially disturbing feature of the present parameterizations is that $f_{OO}<0$, which is difficult to reconcile with known O-O potentials.[20] We do not believe this to be significant, since empirical valence force parameters should only be viewed as "effective" quantities. The negative values of f_{OO} do not lead to any unphysical results. The few attempts we made to constrain $f_{OO}>0$ and to eliminate the small remaining discrepancies in the E_u modes (e.g., by allowing inequivalent angles about O and Pd sites to have different force constants) proved unsuccessful. We eventually abandoned this effort in the interest of simplicity.

Figures 10(a)–10(c) show the densities of states associated with models 1–3, respectively. The results were obtained using 106 200 **k** points in the irreducible Brillouin zone, and the plots are done with an energy resolution of 1 cm^{-1}. The main qualitative features of the spectra are the same in each case. The density of states is divided into two regions with the dominant lower and upper peaks occurring near 150 and 550 cm^{-1}. In Fig. 10(b), the results for a $Pd^{18}O$ crystal are also displayed as the dashed curve. These results indicate that the upper region is primarily associated with O vibrations and the lower region with Pd vibrations. The finer details of the densities of states are less robust and could be further influenced by additional force constants that have no effect on the fit to zone-center modes (e.g., a second-neighbor O-O stretching force). In the analysis to follow, we focus primarily on model 2 for reasons that will become clear shortly.

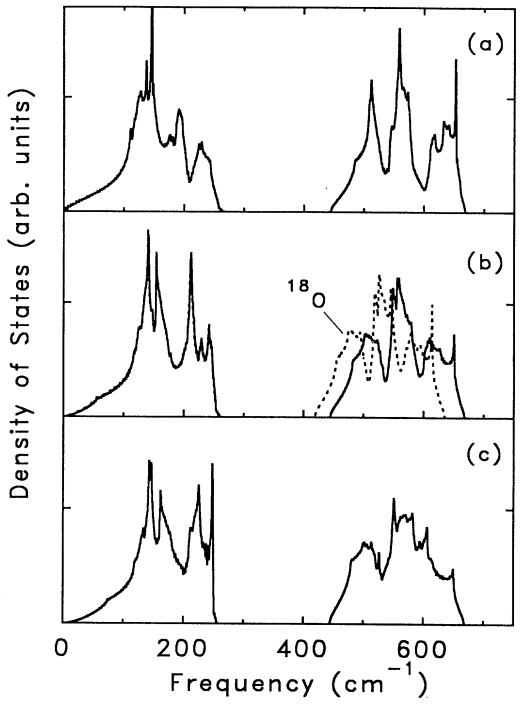

FIG. 10. Calculated density of states for different models described in the text. The dashed curve in (b) is for $Pd^{18}O$. (a), (b), and (c) correspond to models 1, 2, and 3, respectively, of Table I.

Figure 11 shows the phonon dispersion curves calculated with model 2. The frequencies of the lowest-lying modes at X and Z are proportional to $(k_O)^{1/2}$ and are therefore zero in model 1. All of the zone-center modes exhibit significant dispersion as the wave vector increases. Structure in the density of states arises from critical points in the dispersion relations. The peaks in Fig. 10 are associated primarily with the saddle points at X and Z. Eigenvalues at these points and at Γ are listed in Table II, along with the symmetries and isotope shifts of the modes. Since there is no standard convention for labeling the phonon symmetries for a nonsymmorphic space group at points on the surface of the Brillouin zone, we have chosen to designate each phonon symmetry with the **k**-space point plus a subscript representing the order in which that symmetry occurs in the appropriate character table as given by Casher *et al.*[21] The phonon symmetries are determined by operating on the eigenvectors with the operations of the group of the wave vector **k**. At X ($\mathbf{k}=\hat{\mathbf{x}}\pi/a$), the character table is simply that for the D_{2h} point group. All modes are nondegenerate and parity is a good quantum number, i.e., subscripts 1–4 (5–8)

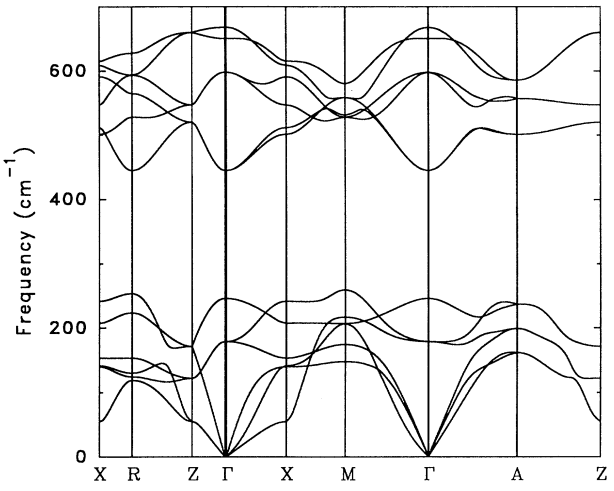

FIG. 11. Phonon dispersion curves for PdO calculated using model 2.

correspond to g (u) modes. At Z ($\mathbf{k}=\hat{\mathbf{z}}\pi/c$), all the irreducible representations are doubly degenerate and parity is not a good quantum number. The double degeneracy of all the modes at Z is evident in Fig. 11, and this behavior persists along the line from Z to A ($\mathbf{k}=\hat{\mathbf{x}}\pi/a+\hat{\mathbf{y}}\pi/a+\hat{\mathbf{z}}\pi/c$). The longitudinal or transverse characters are given for the modes that have pure polarizations.

TABLE II. Eigenvalues for model 2 at Γ, X, and Z.

k-point	Symmetry	Frequency (cm^{-1})	Isotope shift (cm^{-1})
Γ	A_{2u}, E_u	0	0
	E_u^1	179	0
	B_{2u}	246	0
	E_g	445	−25
	E_u^2	598	−28
	B_{1g}	651	−38
	A_{2u}	668	−33
X	X_7(TA)	55	−1
	X_8(LA)	140	0
	X_6(TA)	142	−1
	X_2(TO)	154	0
	X_3	208	−1
	X_1	242	0
	X_3	502	−27
	X_4(TO)	512	−29
	X_7(TO)	547	−24
	X_8(LO)	591	−33
	X_6(TO)	609	−31
	X_1	615	−34
Z	Z_4(TA)	55	−1
	Z_3(TO)	122	0
	Z_1(LA,LO)	172	−1
	Z_3(TO)	520	−28
	Z_4(TO)	547	−24
	Z_1(LO)	660	−35

VI. SECOND-ORDER SCATTERING

A full calculation of the second-order Raman spectrum is very complex and to our knowledge has been discussed in detail only for structures with cubic symmetry such as diamond,[22] rock salt,[22] fluorite,[23] or zincblende.[24] The general procedure involves expressing the symmetry of each phonon branch in terms of the irreducible representations of the group of the wave vector $\mathbf{k}$. The two-phonon joint density of states must first be calculated and then selection rules applied to eliminate forbidden combinations. The number of formally allowed transitions is quite large. However, as pointed out by Cardona,[24] the scattering is typically dominated by those phonon combinations whose irreducible representations contain the identity representation. Since all overtones fall into this category, it is often reasonable to approximate the second-order Raman spectrum by the one-phonon density of states with the energy axis multiplied by two. More precisely, we expect such an overtone density of states to correctly describe the *positions* of most features in the spectrum, but not necessarily their relative *strengths*. The latter depend as well on differences in matrix elements. These differences are neglected here, although we realize that they may be particularly important near a resonance.

In Fig. 12 the overtone density of states calculated

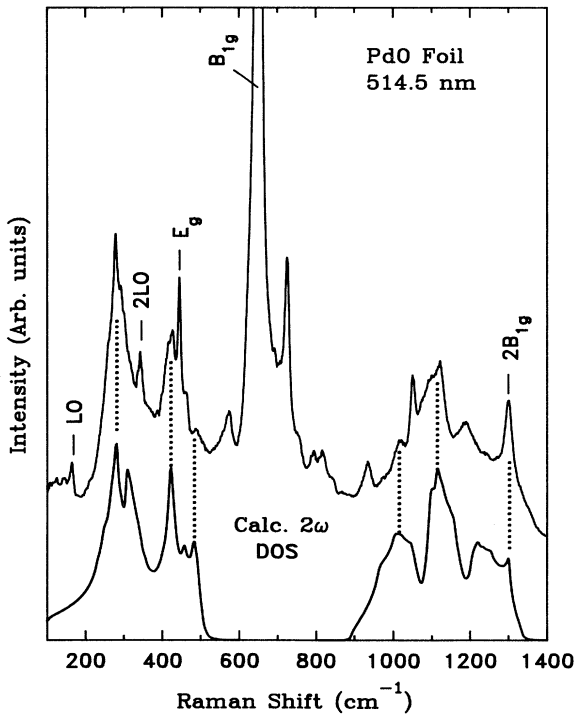

FIG. 12. Calculated 2ω density of states from model 2, lower curve, compared with the observed PdO spectrum, upper curve. The calculated curve has been broadened by 6 cm^{-1} (FWHM) to approximate the experimental resolution.

from model 2 is compared with an experimental spectrum. The density of states results have been Lorentz broadened by 6 cm^{-1} (FWHM), which is approximately the experimental resolution. As anticipated above, there is indeed good agreement, indicated by the vertical dotted lines, between several of the major features in the two curves. Our choice of model 2 was based on its much better fit to the two prominent peaks at 280 and 425 cm^{-1}.

In the low-frequency region, the second-order Raman spectrum is fit remarkably well by the calculated overtone density of states. Between 500 and 900 cm^{-1}, however, there is no overtone contribution, and we conclude that the features here arise from combinations. In the high-frequency region, the general shape of the spectrum is fit fairly well, but some of the details are not present, for example, the peaks at 935, 1051, and 1187 cm^{-1}. These may arise from combinations or they may simply indicate deficiencies in the model. Certainly errors on the order of tens of inverse centimeters are expected in view of the neglect of long-range Coulomb interactions in the calculations. The higher-frequency region is more sensitive to quantitative errors in the model because of the smaller effective masses of the vibrations.

We were able to make assignments for most of the overtone and combination features in the spectrum using only the eigenvalues from the high-symmetry points in the zone listed in Table II. Our choices were constrained by symmetry restrictions and observed isotope shifts. For example, the two assigned combinations involve modes of the same symmetry, which therefore contain the identity representation. One of these, the sharp line at 725 cm^{-1}, appears as the most prominent peak in the spectrum aside from the allowed Raman modes. This line is assigned to the $X_8(LA)+X_8(LO)$ combination, which is predicted to occur at 731 cm^{-1} and have an isotope shift of -33 cm^{-1}, both values being in good agreement with the observations.

The assignments are summarized in Table III, where we have also listed the frequencies and predominant polarizations of the observed features in our spectra. Note that all of the overtones and combinations in the spectra appear only in the polarized scattering geometries $x'x'$ or zz. Although most of these peaks can be seen in both scattering geometries, they tend to be an order of magnitude larger in one or the other. The features in the table that have not been assigned may derive from combinations at other points in the zone. We have made no attempt to fit these, however, due to the limited accuracy of our model.

The two-phonon peak in the spectrum at 1300 cm^{-1}, labeled as $2B_{1g}$ in Fig. 12, is an interesting case and warrants special discussion. Under most circumstances, overtones of the Raman modes are not observed since the density of states goes to zero at the zone center. In PdO, however, we always observe a sharp, polarized (Γ_1^+ symmetry) line at twice the frequency of the B_{1g} mode. A similar phenomenon was seen in diamond (a sharp line appears at roughly twice the frequency of the allowed Raman mode),[25] but not in other materials with the same crystal structure such as silicon and germanium. The two-phonon peak in diamond is actually observed ~ 2

TABLE III. Summary of PdO spectral frequencies and assignments.

Frequency (cm^{-1})	Isotope shift Obs.	Isotope shift Calc.	Assignment, predominant polarization, and comments
165	0	0	E_u^1 LO(Γ); $x'x'$; weak and narrow
278	0	0	$2X_8$(LA) and $2X_6$(TA); $x'x'$; strong broad peak with
292	0	−2	high-frequency shoulder
343	0	0	$2E_u^1$ LO(Γ); zz; narrow
425	0	−1	$2X_3$; $x'x'$; broad
462	0		zz; obscured in $Pd^{16}O$ by the E_g mode
485	0	0	$2X_1$; very weak
445	−25	−25	$E_g(\Gamma)$; $x'z$; very narrow, overlaps 425 cm^{-1} in $Pd^{18}O$
573		−25	X_7(TA)+X_7(TO) or Z_4(TA)+Z_4(TO); zz; obscured in $Pd^{18}O$ by the B_{1g} mode
628		−28	E_u^2 LO(Γ); $x'x'$; extremely weak, observed in $Pd^{16}O$ crystal with the B_{1g} mode extinguished
651	−38	−37	$B_{1g}(\Gamma)$; $x'y'$ or xx; very strong and narrow
678		−33	A_{2u} LO(Γ); $x'x'$; weak, observed in $Pd^{16}O$ crystal with the B_{1g} mode extinguished, overlapped in $Pd^{18}O$
725	−31	−33	$X_8(LA)+X_8(LO)$; $x'x'$; strong and sharp, present in all spectra
794			
817			
935	−37		zz
1017	−53		zz
1051	−55	−56	$2Z_3$(TO); zz; narrow
1122	−68		zz
1187	−74		zz
1300	−75	−75	$2B_{1g}(\Gamma)$; zz; strong

cm^{-1} above twice the one-phonon frequency. Because of this shift, the peak was first attributed to a two-phonon bound state, which would necessarily lie *above* twice the highest phonon frequency.[26] An alternative explanation, which is now generally accepted, is that the peak in diamond is due to the upward curvature of at least some phonon branches near Γ.[27,28] The origin of the shift is still controversial but most likely involves some degree of anharmonicity. In PdO, the two-phonon peak falls well *below* twice the highest phonon frequency and its position agrees with a peak in the overtone density of states. The calculated B_{1g} energy surface for PdO has a saddle point at Γ and is very flat, changing by less than 1 cm^{-1} at 0.1 of the distance to the zone boundary in any direction. Consequently, there is a sharp peak in the density of states in the theoretical plots of Fig. 10, and this yields a sharp overtone peak at precisely twice $B_{1g}(\Gamma)$. Unlike the situation in diamond, the peak in the calculated density of states, broadened by the experimental resolution, does not yield the observed relative intensity of the $2B_{1g}$ line. As shown in Fig. 12, the $2B_{1g}$ line is enhanced by about an order of magnitude compared with neighboring overtone features, apparently because of the resonance. Room-temperature peak positions and widths of the B_{1g} and $2B_{1g}$ lines were accurately measured on one of the foil samples at low power using nearby plasma lines for calibration.[29] The results in cm^{-1} (in air) were $\nu=650.0\pm0.5$, $\Delta\nu=6.4\pm1.0$ and $\nu=1300.1\pm1.0$, $\Delta\nu=22.9\pm3.0$ for the positions and widths of the B_{1g} and $2B_{1g}$ modes, respectively. Thus, within our accuracy, the overtone lies at exactly twice the frequency of the first-order peak, and there is no evidence for an anharmonic shift. The factor of 3 ratio between the widths of the overtone and fundamental is similar to that observed for the corresponding peaks in diamond.[30]

It is well known that forbidden LO phonon scattering at Γ can be induced by defects or by Fröhlich interactions.[31] From a Kramers-Kronig analysis of the PdO ir spectra, Kliche[8] reported LO(Γ) phonons at 168, 622, and 678 cm^{-1}. The lowest-frequency phonon, E_u^1 LO(Γ), shows up most clearly in our spectra. In the foil samples, we observe this line near 165 cm^{-1} and its strength is always greatest in $Pd^{18}O$. In the single-crystal and sputtered film samples, this line was either very weak or nonexistent. The $2E_u^1$ LO(Γ) overtone, which is Raman allowed, was observed as a sharp line in all the samples near 340 cm^{-1}. We were unable to observe the other two LO phonons in the polycrystalline $Pd^{16}O$ samples because of the strong B_{1g} line at 651 cm^{-1}. In the $Pd^{18}O$ foils, however, the B_{1g} mode shifts relatively further than the LO phonons, allowing us to resolve the A_{2u} LO(Γ) phonon as the shoulder at 638 cm^{-1} shown in Fig. 9. We might expect to observe the two higher-frequency LO phonons in single-crystal PdO samples, since we can choose the scattering geometry so as to extinguish the B_{1g} line. This is difficult to accomplish in practice, since the LO phonons are so weak in the crystal and it is nearly impossible to completely extinguish the strong Raman line. However, we do observe a small peak at 678 cm^{-1} and an extremely weak shoulder at 628 cm^{-1} in the $x'x'$ spectra shown in Fig. 5, which may be attributed to the A_{2u} LO(Γ) and E_u^2 LO(Γ) phonons.

VII. DISCUSSION

The most interesting experimental result is the observation of the strong resonance enhancement discussed in Sec. IV B. It is only because of this resonance that we are able to obtain high-quality second-order spectra in an opaque material with a sampling depth of only ~ 100 Å. Although we chose to characterize the resonance with a phenomenological exciton model, there is no definitive evidence to support the existence of a localized exciton state in PdO. On the other hand, the optical data on PdO are suggestive of such a state, as noted by Nilsson and Shivaraman.[4] According to Knox,[32] the signature for an exciton state is a peak in Im(ϵ) just below a band edge. There is indeed a sharp peak in Im(ϵ) for PdO, as shown in Fig. 13, that correlates well with our resonance results. Here we have plotted the optical data along with a Lorentzian line calculated using the parameters from our resonance profiles. Note that the position and width of the calculated line agrees well with the observed peak in Im(ϵ).

In order to resolve the question of whether an excitonic state is responsible for the observed Raman resonance in PdO, a more detailed understanding of the electronic structure is required. A preliminary band-structure calculation for PdO has recently been performed by Carlsson using a density-functional approach.[33] The results show a small (a few tenths of an eV) direct gap at the M point ($\mathbf{k}=\hat{\mathbf{x}}\pi/a+\hat{\mathbf{y}}\pi/a$), with a much larger valence to conduction-band separation in the rest of the zone ($\sim 2-3$ eV). These calculations strengthen the qualitative conclusions derived from the optical data: the

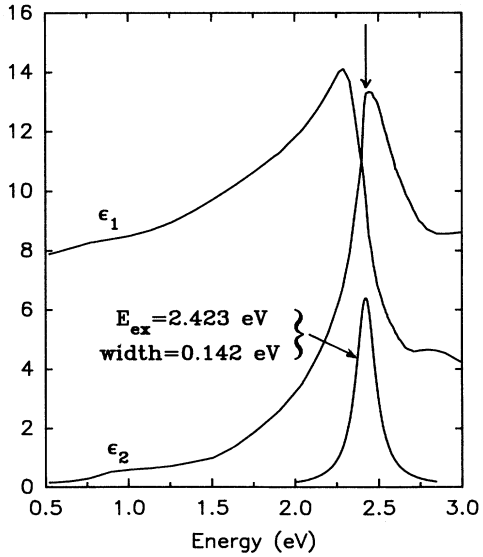

FIG. 13. PdO optical data from Nilsson and Shivaraman, plotted with a Lorentzian curve (in arbitrary units) derived from the resonance Raman profiles. The arrow at the top is aligned with the peak of the Lorentzian for reference.

weak onset of absorption at 0.8 eV is associated with the minimum band gap and that the peak near 2.5 eV may have an excitonic origin. Dare-Edwards *et al.*[11] have attributed this peak to a charge-transfer excitation from the O $2p$ states to the antibonding Pd $4d$ states of local symmetry b_{1g}. Although this simple physical picture is suggestive of an exciton, it is conceivable that a full calculation of $\mathrm{Im}(\epsilon)$ based on band structure alone might be sufficient to explain the sharp peak at 2.5 eV.

In summary, we have performed Raman experiments on a variety of samples and presented lattice dynamics calculations that have allowed us to assign the Raman modes, forbidden LO phonons, and most of the second-order scattering from PdO. In addition, we have measured the resonance profiles of the allowed Raman modes, fit the results to an exciton model, and demonstrated a strong correlation with the optical data. Further work on the electronic structure of PdO is needed to fully understand the resonance effects we have observed.

ACKNOWLEDGMENTS

We thank B. D. Poindexter for his aid in obtaining the Raman spectra and for growing the $Pd^{18}O$ films, R. J. Baird for assistance with the crystal growth, C. R. Peters for the Laue photographs, G. W. Graham for participating in the initial phases of this work, and A. E. Carlsson for communicating to us his preliminary band-structure calculations.

APPENDIX: DYNAMICAL MATRIX

The general form of the dynamical matrix for wave vector $\mathbf{q}$ is

$$D_{\alpha\beta}(\nu'\nu|\mathbf{q})=(M_\nu M_{\nu'})^{-1/2}\sum_j \phi_{\alpha\beta}(0\nu';j\nu)e^{i\mathbf{q}\cdot[\mathbf{x}(j\nu)-\mathbf{x}(0\nu')]}\ , \tag{A1}$$

where $\alpha,\beta=x,y,z$ represent Cartesian coordinates, $\nu',\nu=1,\ldots,n$ denote the n atoms in a primitive unit cell with masses $M_{\nu'},M_\nu$, $\mathbf{x}(j\nu)$ is the location of the νth atom in the jth unit cell, and

$$\phi_{\alpha\beta}(0\nu';j\nu)=\frac{\partial^2 E}{\partial x_\alpha(0\nu')\partial x_\beta(j\nu)} \tag{A2}$$

is an atomic force constant, derived from the total energy E. In the case of PdO, the dynamical matrix may be written in the form

$$D(\mathbf{q})=\begin{bmatrix} D_{11} & D_{12} & D_{13} & D_{13}^{*} \\ D_{12}^{\dagger} & D_{22} & D_{24}^{*} & D_{24} \\ D_{13}^{\dagger} & \tilde{D}_{24} & D_{33} & D_{34} \\ \tilde{D}_{13} & D_{24}^{\dagger} & D_{34}^{\dagger} & D_{44} \end{bmatrix}\ , \tag{A3}$$

where $*$, $\dagger$, and $\sim$ denote complex conjugate, Hermitian conjugate, and transpose, respectively. Each element in (A3) is itself a 3×3 matrix corresponding to the three Cartesian directions, with the subscripts (1, 2, 3, and 4 denoting, in order, Pd atoms at (0,0,0) and ($a/2$, $a/2$, $c/2$) and O atoms at (0, $a/2$, $c/4$) and (0, $a/2$, $3c/4$).

The procedure for calculating $\phi_{\alpha\beta}(0\nu';j\nu)$ and $D(\mathbf{q})$ in terms of the various valence forces introduced in Sec. V is well known.[19] We will not reproduce here the rather lengthy algebra involved but will simply state the final result. To do this, it is useful to introduce the subsidiary quantities

$$\begin{aligned} U_a&=a^2(4a^2+c^2)^{-1},\quad U_c=U_a c^2/a^2\ , \\ V_a&=a^2(4a^2+2c^2)^{-1},\quad V_c=U_c c^2/a^2\ , \\ W_a&=a^2(20a^2+c^2)^{-1},\quad W_c=W_a c^2/a^2\ , \end{aligned} \tag{A4}$$

and the trigonometric functions

$$\begin{aligned} \bar{C}_x&=\cos(q_x a/2)\ , \\ \bar{C}_y&=\cos(q_y a/2)\ , \\ \bar{C}_z&=\cos(q_z c/2)\ , \\ \bar{S}_x&=\sin(q_x a/2)\ , \\ \bar{S}_y&=\sin(q_y a/2)\ , \\ \bar{S}_z&=\sin(q_z c/2)\ , \\ C_x&=\cos(q_x a)\ , \\ C_y&=\cos(q_y a)\ , \\ S_x&=\sin(q_x a)\ , \\ S_y&=\sin(q_y a)\ . \end{aligned} \tag{A5}$$

The only nonzero elements of (A3) are then

$$\begin{aligned} D_{11}^{xx}&=4\{32W_a f_{\mathrm{PdO}}^2+[2-2V_c+(1-C_x)U_c]k_{\mathrm{O}}+\mu\}/M_{\mathrm{Pd}}\ , \\ D_{11}^{yy}&=4\{4U_a f_{\mathrm{PdO}}^1+8W_a f_{\mathrm{PdO}}^2+[(3-C_y)U_c-2V_c]k_{\mathrm{O}}+2U_c k_{\mathrm{Pd}}\}/M_{\mathrm{Pd}}\ , \\ D_{11}^{zz}&=D_{22}^{zz}=4\{U_c f_{\mathrm{PdO}}^1+2W_c f_{\mathrm{PdO}}^1+4[(C_x+C_y)U_a+2U_c V_a]k_{\mathrm{O}}+8U_a k_{\mathrm{Pd}}\}/M_{\mathrm{Pd}}\ , \\ D_{22}^{xx}&=D_{11}^{yy}\quad(\text{with } C_y\rightarrow C_x)\ , \\ D_{22}^{yy}&=D_{11}^{xx}\quad(\text{with } C_x\rightarrow C_y)\ , \end{aligned} \tag{A6}$$

$$
\begin{aligned}
&D_{33}^{xx}=D_{44}^{xx}=[8U_a f_{\mathrm{PdO}}^{1}+80W_a f_{\mathrm{PdO}}^{2}+4(1+U_c)k_{\mathrm{O}}+2U_c(2-C_x)k_{\mathrm{Pd}}+\mu]/M_{\mathrm{O}}\ ,\\
&D_{33}^{yy}=D_{44}^{yy}=D_{33}^{xx}\ \ (\text{with } C_x\rightarrow C_y)\ ,\\
&D_{33}^{zz}=D_{44}^{zz}=2[2U_c f_{\mathrm{PdO}}^{1}+4W_c f_{\mathrm{PdO}}^{2}+f_{\mathrm{OO}}+16U_a k_{\mathrm{O}}+4U_a(4+C_x+C_y)k_{\mathrm{Pd}}]/M_{\mathrm{O}}\ ,\\
&D_{33}^{xz}=(D_{33}^{zx})^{*}=-D_{44}^{xz}=-(D_{44}^{zx})^{*}=4i\sqrt{U_a U_c}S_x k_{\mathrm{Pd}}/M_{\mathrm{O}}\ ,\\
&D_{33}^{yz}=(D_{33}^{zy})^{*}=-D_{44}^{yz}=-(D_{44}^{zy})^{*}=4i\sqrt{U_a U_c}S_y k_{\mathrm{Pd}}/M_{\mathrm{O}}\ ,
\end{aligned}
\tag{A7}
$$

$$
D_{12}=\left[8\frac{k_{\mathrm{O}}}{M_{\mathrm{Pd}}}\right]\begin{vmatrix} V_c\bar{C}_x\bar{C}_y\bar{C}_z & (V_a/U_a)\bar{S}_x\bar{S}_y\bar{C}_z & 2\sqrt{V_a V_c}\bar{S}_x\bar{C}_y\bar{S}_z \\ U_c V_c\bar{S}_x\bar{S}_y\bar{C}_z & V_c\bar{C}_x\bar{C}_y\bar{C}_z & -2U_c V_c\left[\frac{a}{c}\right]\bar{C}_x\bar{S}_y\bar{S}_z \\ -2U_c V_c\left[\frac{a}{c}\right]\bar{S}_x\bar{C}_y\bar{S}_z & 2\sqrt{V_a V_c}\bar{C}_x\bar{S}_y\bar{S}_z & -4U_c V_a\bar{C}_x\bar{C}_y\bar{C}_z \end{vmatrix}
\tag{A8}
$$

$$
\begin{aligned}
&D_{34}^{xx}=(2U_c e^{iq_z c/2}k_{\mathrm{Pd}}+C_y e^{-iq_z c/2}\mu)/M_{\mathrm{O}}\ ,\\
&D_{34}^{yy}=(D_{34}^{xx})^{*}\ \ (\text{with } C_y\rightarrow C_x)\ ,\\
&D_{34}^{zz}=-2\bar{C}_z(f_{\mathrm{OO}}+8U_a k_{\mathrm{Pd}})/M_{\mathrm{O}}\ ,
\end{aligned}
\tag{A9}
$$

$$
\begin{aligned}
&D_{13}^{xx}=-2\bar{C}_y e^{iq_z c/4}(32W_a C_x f_{\mathrm{PdO}}^{2}+2k_{\mathrm{O}}+\mu)/\sqrt{M_{\mathrm{O}}M_{\mathrm{Pd}}}\ ,\\
&D_{13}^{yy}=-4\bar{C}_y e^{iq_z c/4}[2U_a f_{\mathrm{PdO}}^{1}+4W_a C_x f_{\mathrm{PdO}}^{2}+U_c(k_{\mathrm{O}}+k_{\mathrm{Pd}})]/\sqrt{M_{\mathrm{O}}M_{\mathrm{Pd}}}\ ,\\
&D_{13}^{zz}=-2\bar{C}_y e^{iq_z c/4}[U_c f_{\mathrm{PdO}}^{1}+2W_c C_x f_{\mathrm{PdO}}^{2}+8U_a(k_{\mathrm{O}}+k_{\mathrm{Pd}})]/\sqrt{M_{\mathrm{O}}M_{\mathrm{Pd}}}\ ,\\
&D_{13}^{xy}=D_{13}^{yx}=32W_a S_x\bar{S}_y e^{iq_z c/4}f_{\mathrm{PdO}}^{2}/\sqrt{M_{\mathrm{O}}M_{\mathrm{Pd}}}\ ,\\
&D_{13}^{xz}=D_{13}^{zx}=-16iS_x\bar{C}_y e^{iq_z c/4}\sqrt{W_a W_c}f_{\mathrm{PdO}}^{2}/\sqrt{M_{\mathrm{O}}M_{\mathrm{Pd}}}\ ,\\
&D_{13}^{yz}=D_{13}^{zy}=-4i\bar{S}_y e^{iq_z c/4}[\sqrt{U_a U_c}(f_{\mathrm{PdO}}^{1}-2k_{\mathrm{O}}-2k_{\mathrm{Pd}})+2\sqrt{W_a W_c}C_x f_{\mathrm{PdO}}^{2}]/\sqrt{M_{\mathrm{O}}M_{\mathrm{Pd}}}\ ,
\end{aligned}
\tag{A10}
$$

and

$$
D_{24}=D_{13}\ \ (\text{with } x\leftrightarrow y \text{ interchanged})\ . \tag{A11}
$$

The eigenvalues of $D(\mathbf{q})$ correspond to the squares of the phonon frequencies at wave vector $\mathbf{q}$. For certain high-symmetry states, the required diagonalization is easily carried out analytically. The following expressions for three of the modes at Γ were thus used to simplify the parameterizations in Sec. V:

$$
\begin{aligned}
&\omega^2(E_g)=4[2U_a f_{\mathrm{PdO}}^{1}+20W_a f_{\mathrm{PdO}}^{2}+(1+U_c)k_{\mathrm{O}}]/M_{\mathrm{O}}\ ,\\
&\omega^2(B_{1g})\\
&\quad=4[U_c f_{\mathrm{PdO}}^{1}+2W_c f_{\mathrm{PdO}}^{2}+8U_a(k_{\mathrm{O}}+2k_{\mathrm{Pd}})+f_{\mathrm{OO}}]/M_{\mathrm{O}}\ ,\\
&\omega^2(A_{2u})=4[U_c f_{\mathrm{PdO}}^{1}+2W_c f_{\mathrm{PdO}}^{2}+8U_a(k_{\mathrm{O}}+k_{\mathrm{Pd}})]\\
&\qquad\times[(M_{\mathrm{O}})^{-1}+(M_{\mathrm{Pd}})^{-1}]\ .
\end{aligned}
\tag{A12}
$$

[1]H. Okamoto and T. Aso, Jpn. J. Appl. Phys. **6**, 779 (1967).
[2]D. B. Rogers, R. D. Shannon, and J. L. Gillson, J. Solid State Chem. **3**, 314 (1971).
[3]E. Rey, M. R. Kamal, R. B. Miles, and B. S. H. Royce, J. Mater. Sci. **13**, 812 (1978).
[4]P. O. Nilsson and M. S. Shivaraman, J. Phys. C **12**, 1423 (1979).
[5]H. Hagermann, H. Bill, W. Sadowski, E. Walker, and M. François, Solid State Commun. **73**, 447 (1990).
[6]J. C. Irwin, J. Chrzanowsky, T. Wei, D. J. Lockwood, and A. Wold, Physica C **166**, 486 (1990).
[7]G. Kliche and Z. V. Popovic, Phys. Rev. B **42**, 10 060 (1990).
[8]G. Kliche, Infrared Phys. **25**, 381 (1985).
[9]W. H. Weber, R. J. Baird, and G. W. Graham, J. Raman Spectrosc. **19**, 239 (1988).
[10]G. Kliche, Z. Naturforsch. A **44**, 169 (1989).
[11]M. P. Dare-Edwards, J. B. Goodenough, and A. Hamnett, Mater. Res. Bull. **19**, 435 (1984).
[12]R. W. G. Wyckoff, *Crystal Structures,* 2nd ed. (Interscience, New York, 1964), Vol. 1, pp. 139–140.
[13]B. H. Brandow, Adv. Phys. **26**, 650 (1977).
[14]S. G. Gagarin, A. L. Gubskii, A. P. Kovtun, A. A. Krichko, and V. P. Sachenko, Kinet. Catal. **23**, 491 (1982).
[15]Y. Holl, G. Krill, A. Amamou, P. Légaré, L. Hilaire, and G. Maire, Solid State Commun. **32**, 1189 (1979).
[16]See, for example, G. W. Ford and W. H. Weber, Phys. Rep. **113**, 195 (1984).
[17]A. K. Ganguly and J. L. Birman, Phys. Rev. **162**, 806 (1967).
[18]The bond-bending force constants are defined so that an angu-

lar change of $\Delta\theta$ (in rad) increases the energy by $\frac{1}{2}k(d\Delta\theta)^2$, where $k=k_O$ or k_{Pd} and d is the Pd-O bond length (2.024 Å). For a Pd atom and its four O neighbors (labeled 1–4 in order along the periphery) in the xz plane, we define the buckling force constant μ to be that associated with an energy $\mu\{[u_y^{Pd}-(u_{1y}+u_{3y})/2]^2+[u_y^{Pd}-(u_{2y}+u_{4y})/2]^2\}$, where u_y^{Pd} and u_{iy} ($i=1,4$) are the y displacements of the Pd atom and its ith O neighbor, respectively.

[19]P. Brüesch, in *Phonons: Theory and Experiments I,* Vol. 34 of *Springer Series in Solid-State Sciences,* edited by P. Fulde, (Springer-Verlag, Berlin, 1982).

[20]A. I. Kitaigorodsky, *Molecular Crystals and Molecules* (Academic, New York, 1973).

[21]A. Casher, M. Glück, and Y. Gur, in *The Irreducible Representations of Space Groups,* edited by J. Zak (Benjamin, New York, 1969).

[22]See, for example, J. L. Birman, *Theory of Crystal Space Groups and Lattice Dynamics* (Springer-Verlag, Berlin, 1984), Chaps. M and N.

[23]N. Krishnamurthy and V. Soots, Can. J. Phys. **50**, 849 (1972).

[24]M. Cardona, in *Light Scattering in Solids II,* Vol. 50 in *Topics in Applied Physics,* edited by M. Cardona and G. Güntherodt (Springer-Verlag, Berlin, 1982), pp. 62–69.

[25]S. A. Solin and A. K. Ramdas, Phys. Rev. B **1**, 1687 (1970).

[26]M. H. Cohen and J. Ruvalds, Phys. Rev. Lett. **23**, 1378 (1969).

[27]R. Tubino and J. L. Birman, Phys. Rev. B **15**, 5843 (1977).

[28]C. Z. Wang, C. T. Chan, and K. M. Ho, Solid State Commun. **76**, 483 (1990).

[29]N. C. Craig and I. W. Levin, Appl. Spectrosc. **33**, 475 (1979).

[30]M. A. Washington and H. Z. Cummins, Phys. Rev. B **15**, 5840 (1977).

[31]See M. Cardona, *Light Scattering in Solids II,* Ref. 24, pp. 128–135.

[32]R. S. Knox, in *Theory of Excitons,* Suppl. 5 in *Solid State Physics,* edited by F. Seitz and D. Turnbull (Academic, New York, 1963), Chap. 9.

[33]A. E. Carlsson (private communication).

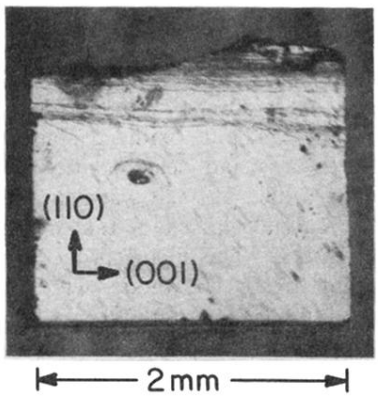

FIG. 1. Photograph of PdO crystal with large (110) face.